Terminal Deuterium Atoms Protect Silicon from Oxidation

Tiexin Li [a], Chandramalika R. Peiris [a], Albert C. Aragonès [b,c], Carlos Hurtado [a], Anthony Kicic [d, e, f, g], Simone Ciampi [a], Melanie MacGregor [h], Tamim Darwish [i], Nadim Darwish [a]*

a School of Molecular and Life Sciences, Curtin University, Bentley, WA 6102, Australia
b Departament de Ciència de Materials i Química Física, Universitat de Barcelona, Marti i Franquès 1, 08028 Barcelona, Spain
[c] Institut de Química Teòrica i Computacional (IQTC), Universitat de Barcelona, Diagonal 645, 08028 Barcelona, Spain
[d] Occupation, Environment and Safety, School of Population Health, Curtin University, Bentley, WA, 6102, Australia
[e] Wal-Yan Respiratory Research Centre, Telethon Kids Institute, The University of Western Australia, Nedlands, WA, 6009, Australia
[f] Department of Respiratory and Sleep Medicine, Perth Children's Hospital, Nedlands, WA, 6009, Australia
[g] Centre for Cell Therapy and Regenerative Medicine, The University of Western Australia, Nedlands, WA, 6009, Australia
[h] Flinders Institute for Nanoscale Science & Technology, Flinders University, Bedford Park, SA 5042, Australia
[i] National Deuteration Facility, Australian Nuclear Science and Technology Organisation (ANSTO), New Illawarra Road, Lucas Heights, NSW 2234, Australia

*Corresponding author: nadim.darwish@curtin.edu.au

ABSTRACT

In recent years, the hybrid silicon-molecular electronics technology has been gaining significant attention for applications in sensors, photovoltaics, power-generation and molecular electronics devices. However, Si–H surfaces, which are the platform on which these devices are formed, are prone to oxidation, compromising the mechanical and electronic stability of the devices. Here, we show that when hydrogen is replaced by deuterium, the Si–D surface become significantly more resistant to oxidation when either positive or negative voltages are applied to the Si surface. Si–D surfaces are more resistant to oxidation and their current–voltage characteristics are more stable than those measured on Si–H surfaces. At positive voltages, the Si–D stability appears to be related to the flat band potential of Si–D being more positive compared to Si–H surfaces, making Si–D surfaces less attractive to oxidizing OH^- ions. The limited oxidation of Si–D surfaces at negative potentials is interpreted by the frequencies of the Si–D bending modes being coupled to that of the bulk Si surface phonon modes, which would make the duration of Si–D excited vibrational state significantly less than that of Si–H. The strong surface isotope effect has implications in the design of silicon-based sensing, molecular electronics and power-generation devices, and on the interpretation of charge transfer across them.

Keywords: deuterium, flat band potential, silicon oxidation, surface isotope effect

1. INTRODUCTION

In 1996, Lyding performed scanning tunnelling microscopy (STM) experiments to stimulate hydrogen desorption from Si surfaces and found that it was about 100 times more difficult to remove a deuterium atom than it was to remove a hydrogen atom from Si surfaces.[1] More recently, it has been shown that the lifetime of metal–oxide–semiconductor transistors increased when H was replaced by D at the interface of Si/SiO_2.[2-6] The strong isotope effect on Si surfaces is owed to the Si–D bond being more resistant to electron excitation in comparison with Si–H bonds.[7, 8] Since the static electronic structure of the Si–H and Si–D bonds is similar, the strong surface isotope effect is related to dynamics.[9-12] Shen *et al.* proposed that the STM induced desorption of hydrogen atoms from Si proceeds via a multiple-vibrational excitation by tunnelling electrons.[13] Electrons excite Si–H vibrational transitions with a rate proportional to the tunnelling current. The extent to which vibrational energy can be stored in the bond depends on the lifetime, i.e., on the rate at which energy is lost by coupling to bulk silicon phonons. Van de Walle *et al.* proposed that both the vibrational lifetime and dissociation mechanism are controlled by the Si–H versus Si–D bending modes.[14] They proposed that the bending modes of Si–D are coupled to bulk Si phonon states. This is because the frequencies of the bending modes for Si–D is theoretically expected to be closer to the bulk Si phonon states than that of Si–H. The coupling of Si–D bending modes to the bulk Si phonons result in an efficient channel for de-excitation. Therefore, it is expected that it will be more difficult for Si–D to reach a highly excited vibrational state that Si–H. Deuterium should therefore be much more difficult to be removed from the Si surface. However, these predictions were only supported by low temperature STM experiments, and the effect of the H vs D desorption on the oxidation of practical Si devices, on the electrochemical rates when Si is bound to redox species (e.g., those used in chemical and biosensors), and on Si current–voltage characteristics (e.g., those used in molecular electronics) remains unknown.

In recent years, there is increasing interest in modifying Si with organic monolayers to form a hybrid technology that combine the semiconducting properties of silicon with properties of organic molecules.[15-24] The applications of this technology includes sensors,[25-27] photovoltaics,[28-33] and molecular electronics devices.[34-37] In most of these applications, the typical procedure is first to remove the natural oxide layer that forms on the Si surface to expose the reactive Si–H surface. The Si–H surface is then reacted via a hyrdosilylation reaction mainly with alkenes or alkynes.[21, 38-47] The reaction yields an organic monolayer of density ~ 50% and the remaining unreacted sites stay as Si–H. These Si–H sites are reactive towards oxygen and water and initiate an oxidation of the silicon surface.[39] The oxide layer grows on the surface of the silicon atoms and in between the Si atoms of the surface, change Si–Si bond angles, break bonds and extend inside the bulk Si structure. The mechanism of oxidation of Si surfaces is a subject to continuous debate. While at positive potentials, it is believed that OH^- reacts with the Si surface, it is less clear how oxidation happens at negative potentials. A possible explanation for negative potential oxidation is that the current-induced dissociation of the Si–H bonds creates radicals which then react with molecular oxygen that initiates oxidation.[48] This oxidation has a detrimental effect on Si devices. For example, oxidation can desorb the monolayer, thereby changing the conductivity and the rate of electron transfer at the interface – a typical measurement used for sensing applications.[25] As a consequence, there has been increasing interest in either avoiding or preventing the re-growth of the insulating oxide layer on bare silicon electrodes. These efforts include forming molecular films with dense polymeric structures, or by using impermeable 2D materials, such as graphene or graphene oxide to protect Si from oxidation.[49] In 1998, Luo and Chidsey first reported the method of deuterium-terminated silicon surfaces by using a solution of KF and DCl in D_2O.[50] Since then, several papers utilizing this method have been reported.[51-53]

In this study, we compare Si–H and Si–D surfaces, in terms of their ability to resist oxidation and how this affect the conductivity and the rate of electron transfer across the Si surface at positive and negative voltage-biases. The biases were supplied either by potentiostat in a wet electrochemical experiments or by using conducting atomic force microscopy on a monolayer formed from nonadiyne on Si. Cyclic voltammetry (CV) and electrochemical impedance spectroscopy (EIS) were then used to determine the molecular surface coverage and electron transfer kinetics. Voltage–current electrical measurements were used to contrast the topography of oxide formed with its conductivity. UV photoelectron spectroscopy (UPS) was used to determine the band edges of the different surfaces. Time-resolved photocurrent mapping was used to determine electron-hole recombination time constant.

2. MATERIALS AND METHODS

2.1 Materials

Unless specified otherwise, all chemicals were of analytical grade and used as received. Chemicals used in surface modification and electrochemical experiments were of high purity (>99%). Milli–Q water (>18 MΩ cm) was used for surface cleaning, glassware cleaning and for the preparation of the electrolyte solutions. Dichloromethane (DCM) and 2–propanol were distilled before use. Hydrogen peroxide

(30 wt% in water) and sulfuric acid (Puranal TM, 95–97%) were used for wafer cleaning. Deuterated water (D_2O), deuterated dichloromethane (CD_2Cl_2), potassium fluoride (KF), and Ammonium fluoride (NH_4F) were purchased from Sigma-Aldrich and used for wafer cleaning and etching to prepare deuterated Si surfaces. 1,8–Nonadiyne (98%) was obtained from Sigma-Aldrich and used as received. Azidomethylferrocene was synthesized from ferrocene methanol as per established procedures.[54] Aqueous perchloric acid (1.0 M) was used as the electrolyte in all electrochemical measurements. Silicon wafers were purchased from Siltronix, S.A.S. (Archamps, France), p-type boron doped, and had a thickness of 500 ± 25 μm and a resistivity of 0.007–0.013 Ω cm.

2.2 Surface Modification

2.2.1 Silicon preparation

Silicon electrodes were cleaned and etched by the following literature procedures.[15, 39, 54, 55] In brief, for Si–D surfaces, silicon wafers were cut into pieces (approximately 1 × 1 cm), cleaned in hot Piranha solution (130 °C, 3:1(v/v) mixture of concentrated sulfuric acid to 30% hydrogen peroxide) for 20 minutes, (**S–2**, Figure 1) then rinsed with water and etched in a solution of anhydrous potassium fluoride (KF) (40 wt% in D_2O) to which were added a few drops of 37% deuterated hydrochloric acid (DCl) and

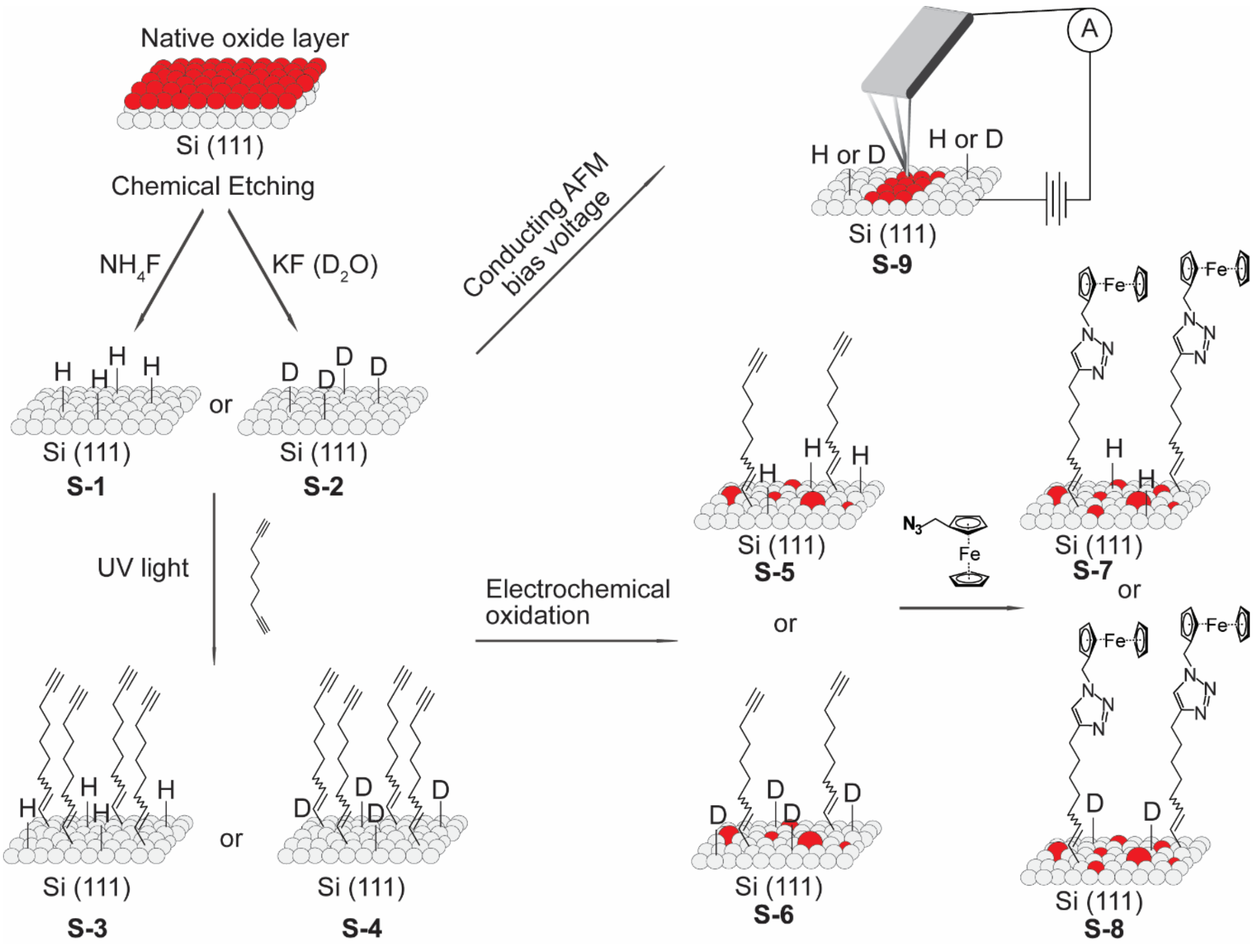

Figure 1. *Schematic of the SAMs studied. Oxide–free silicon (Si–H, Si–D) electrodes (**S–1**, **S–2**) are prepared and then reacted with 1,8-nonadiyne via a hydrosilylation reaction to form SAMs **S–3** and **S–4**. Electrochemical potentials of + 0.6, + 1.0, + 1.5 V, – 0.6 V, – 1.0 V, and –1.5 V are then applied to SAM **S–3** and **S–4** to form SAM **S–5** and **S–6,** respectively. A ferrocene moiety is attached to the distal end of SAMs **S–5** and **S–6** by a copper-catalyzed azide-alkyne "click" reaction to yield the redox-active SAMs **S–7** and **S–8**. On the other hand, C–AFM induced oxidation of SAMs **S–1** and **S–2** were obtained by applying + 0.5, + 2, + 3 and, + 5 V bias-voltage to yield SAM **S–9**. The schematic assumes that the oxide grows progressively from the molecular scale to the nanoscale and then to the microscale.*

a small quantity of anhydrous sodium sulphite under a stream of argon for 13 minutes. The etched surfaces were rinsed with D_2O water and CD_2Cl_2 before being placed in a deoxygenated sample of 1,8–nonadiyne. For Si–H surfaces, a similar procedure was followed except for using the typical ammonium fluoride etching. After cleaning in hot piranha solution (130 ˚C, 3:1(v/v) mixture of concentrated sulfuric acid to 30% hydrogen peroxide) for 20 minutes, (**S–1**, Figure 1) the Si–H surfaces were rinsed with water and etched in deoxygenated (40 wt%) aqueous ammonium fluoride solution under a stream of argon for 13 minutes. The etched surfaces were rinsed with Milli–Q water and CH_2Cl_2 before being placed in a deoxygenated sample of 1,8–nonadiyne. The surfaces (**S–3** and **S–4**, Figure 1) were then rapidly transferred to a glass board which was covered by quartz and kept under positive nitrogen flow pressure, and illuminated with UV light (Vilber, VL–215.M, $\lambda = 312$ nm) for 2 hours.

2.2.2 Electrochemical oxidation

Amperometric I–T measurements were run at different voltage (+ 0.6, + 1, + 1.5, – 0.6, – 1, and – 1.5 V) for 1 minute, 5 minutes, and 10 minutes. The 1,8–nonadiyne SAMs served as working electrode, a platinum wire as the auxiliary electrode, and an Ag/AgCl aqueous electrode (1.0 M KCl, CH Instruments, USA) as the reference electrode. Aqueous 1.0 M perchloric acid was used as the electrolyte.

2.2.3 Copper-catalysed azide–alkyne “click” reaction

The electrochemically oxidized 1,8–nonadiyne SAMs (**S–5** and **S–6**, Figure 1) were reacted with azidomethylferrocene through a copper-catalysed “click” reaction to yield SAMs **S–7** and **S–8**. In brief, **S–5** and **S–6** samples were incubated for 120 minutes in a solution of 0.4 µM copper (II) sulphate pentahydrate, sodium ascorbate (5 mg/mL) and 0.5 mM azidomethylferrocene, under dark conditions. The silicon surfaces were then removed from the solution and washed sequentially with 2-propanol, Milli-Q water, 0.5 M hydrochloric acid, Milli-Q water, 2-propanol and DCM. Finally, the silicon substrates (**S–7** and **S–8**) were blown dry with a stream of argon before analysis.

2.3. Surface characterization

2.3.1 Electrochemical measurements

Electrochemical measurements were carried out in a single-compartment, three-electrode PTFE cell using a CHI650 electrochemical workstation (CH Instruments, USA). The modified silicon surface served as the working electrode, a platinum wire as the auxiliary electrode, and an Ag/AgCl aqueous electrode (1.0 M KCl, CH Instruments, USA) as the reference electrode. Aqueous 1.0 M perchloric acid was used as the electrolyte. The electrical contact between silicon and copper was reached by rapidly rubbing gallium indium eutectic on the back side of the silicon substrate. EIS measurements were carried out with a DC offset equal to the half-wave potential ($E_{1/2}$) measured in the CV experiments. The AC amplitude was 15 mV and the frequency was scanned between 0.1 and 100,000 Hz. The surface coverage (Γ) of ferrocene molecules was calculated from the integration of the CV oxidation waves according to equation: $\Gamma = Q/nFA$, where Q is charge, n is the number of electron transfer, F is the Faraday constant and A is the area of the electrode (cm^{-2}). The out-of-phase impedance (Z'') was used to estimate the electrode capacitance ($C = 1/(\omega Z'')^{-1}$). The capacitance was used to determine the Mott-Schottky plot ($1/C^2$).

2.3.2 Conductive Atomic Force Microscope (C–AFM)

Tip induced oxidation was performed on Bruker Dimension PF–TUNA atomic force microscopy in ambient conditions (21 °C and 30% relative humidity). All images and current–voltage (I–V) curves were obtained with solid Pt tips (RMN–25PT300B, Rocky Mountain Nanotechnology), with nominal spring constant of 18 N/m, nominal resonant frequency of 20 kHz, and tip radius < 20 nm in air at room temperature. The silicon wafers were oxidized by applied biases ranging from 0.5 to 5 V. I–V curves were obtained by ramping 20 times in each position at a peak force of 2.25 µN and 1 Hz ramp rate.

2.3.3 Contact angle analysis

The wettability of the Si surfaces was measured by an automated static water contact angle with a Krüss DSA 100 goniometer. The reported values are the average of at least three droplets, and the error bars represent the standard deviation of three measurements on three different surfaces.

2.3.4 X-ray photoelectron spectroscopy (XPS)

X-ray photoelectron spectroscopy (XPS) analysis of the monolayer-modified silicon surfaces was performed on a Kratos Axis Ultra DLD fitted with a monochromatic Al Kα (hυ1486.6 eV) radiation source operating at 225 W, and a hemispherical analyzer (165 mm radius) running in fixed analyzer transmission mode. The photoelectron take-off angle was normal to the sample, and the chamber operated at 2×10^{-8} Torr. The analysis area was 300 × 700 µm, and an internal flood gun was used to minimize sample charging. Survey spectra (accumulation of three scans) were acquired between 0 and 1100 eV, with a dwell time of 55 ms, a pass energy of 160 eV, and a step size of 0.5 eV. High-resolution scans (accumulation of 10 scans) used a pass energy of 20 eV, and a step size of either 0.05 eV (Si 2p, 90–110 eV), or 0.1 eV (C 1s, 277–300 eV). XPS data were processed in CasaXPS (version 2.3.18) and any residual charging was corrected by applying a rigid shift to bring the main C 1s emission (C–C) to 284.7 eV.

2.3.5 UV photoelectron spectroscopy (UPS)

UPS was used to determine the work function of the surfaces. Details can be found in previous publications. Here we summarize the main features of the method. He I UV light was produced by a metastable helium atom (He* in the $^3S_1$ state) source which emits He* and He I UV light simultaneously from a cold cathode two stage discharge source. Electrons emitted due to the impact of UV photons and He* are separated by a chopper. A bias voltage of 10 V was applied to the sample stage. The excitation energy in the UPS experiments was 21.22 eV.

2.3.6 Time-resolved photocurrent mapping

Spatially resolved measurements of photocurrent decay kinetics (photocurrent mapping, PCM) were performed with a NX10 AFM (Park Systems Corporation) fitted with a PCM module controlling a pulsed red laser (635 nm, 5 mW nominal power output). The laser on/off time was controlled by the Systems SmartScanTM software, and dark C-AFM conditions were ensured by temporarily switching off the AFM tip feedback. The photocurrent acquisition time was set to 20 ms, and a 4 ms laser pulse started after a 3-ms delay from the acquisition start point. No external bias was applied during the measurements. Junctions analyzed in the time resolved PCM experiments were formed by contacting the silicon wafers and AFM platinum tips (25Pt300B) with no relative movement between them. For each sample, PCM measurements were taken at 100 different locations.

3. RESULTS

3.1. X-ray photoelectron spectroscopy (XPS)

Figure 2a and 2d shows the XPS Si 2p narrow scan for freshly prepared surfaces, the surfaces oxidized at – 0.6 V (Figure 2b and e), and the surfaces oxidized at – 1.5 V (Figure 2c and f). For SAM **S–1**, the amount of SiO_x at 102 eV (relative to Si at 98-100 eV) increase from 0% (below detection limit in XPS) to 20.7% and 43.0% when the voltage increased from – 0.6 V (applied for 1 minute) to – 1.5 V (applied for 10 minutes), respectively (Figure 2a-c) (Table S1, Supporting information). On the other hand, the deuterated SAM **S–2** showed an increase from 0% (below detection limit in XPS) to 1.7% and 29.5% when the voltage increased from – 0.6 V (applied for 1 minute) to – 1.5 V (applied for 10 minutes), respectively (Figure 2d-f) (Table S1, Supporting information). The Si 2p high resolution envelope was fitted by two peaks, with the main emission composed of one spin-orbit split with two peaks at 98.85 eV and 99.45 eV, corresponding to the Si $2p_{3/2}$ and Si $2p_{1/2}$ for low and high energy spins, respectively.[56, 57] The XPS survey and O 1s spectra are shown in Figures S1 and S2 (Supporting Information). A similar trend was also obtained when positive voltages were applied to the surfaces (Figure 2g-l).[58, 59] In addition XPS measurements performed on Si–H and Si–D surfaces at ambient conditions showed the Si–D surfaces is advantageous over Si–H surfaces in preventing the oxidation of the surfaces. The results show the oxide increase from 0 % to 18 % and from 0 % to 12 % on Si–H surface and Si–D surface, respectively after 15 days (21 °C and 30% relative humidity). (Supporting Information, Figure S3). The XPS results are consistent with water contact measurements which were lower as a function of the applied voltages for Si–D vs Si–H surfaces (See Supporting Information, Figure S4 and S5).

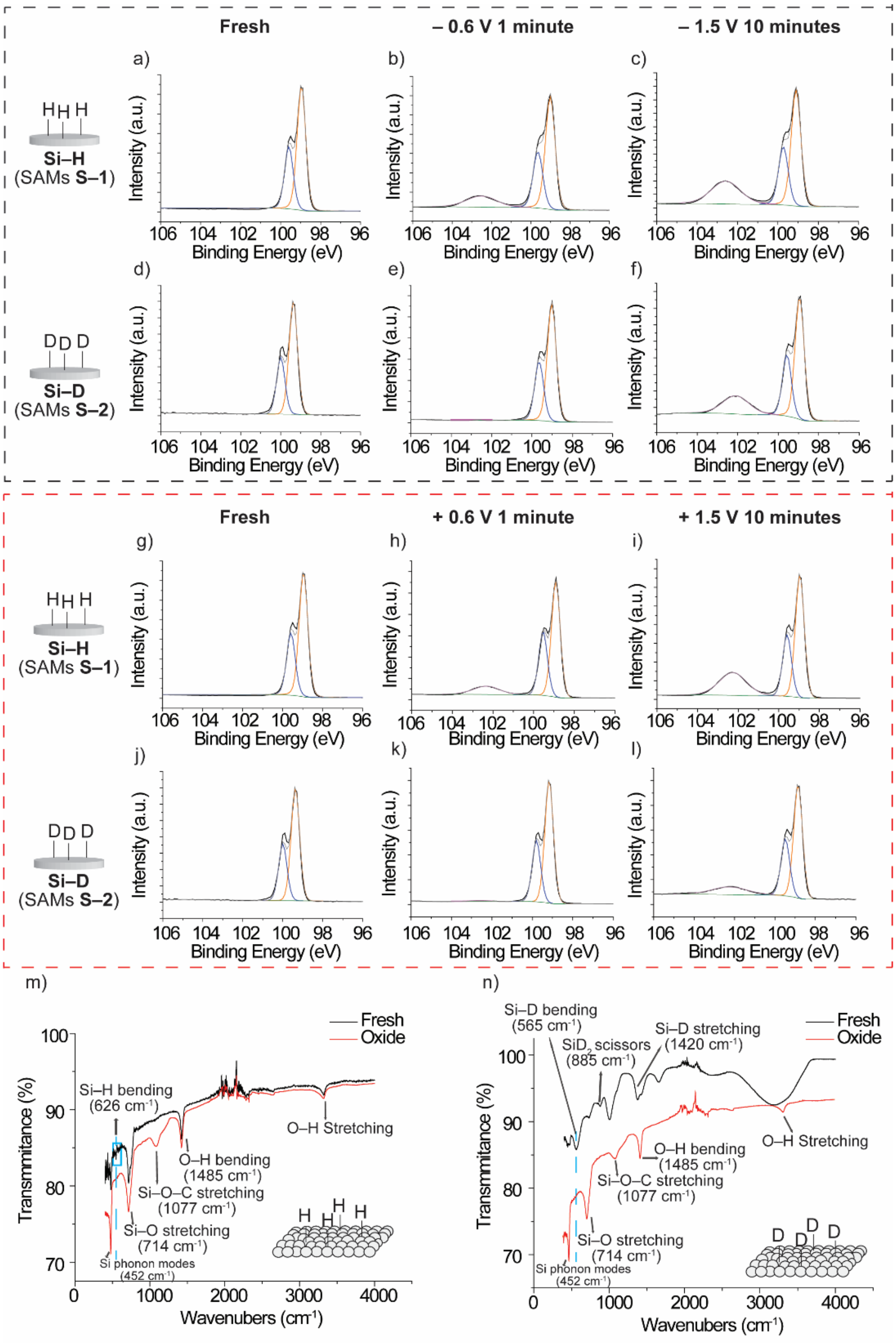

Figure 2. *XPS high resolution Si 2p spectra for SAMs* ***S–1*** *(a) freshly prepared, (b) after oxidation at – 0.6 V, and (c) after oxidation at – 1.5 V. XPS high resolution Si 2p spectra for SAMs* ***S–2*** *(d) freshly prepared, (e) after oxidation at – 0.6 V, and (f) after oxidation at – 1.5 V. XPS high resolution Si 2p spectra for SAMs* ***S–1*** *(g) freshly prepared, (h) after oxidation at + 0.6 V, and (i) after oxidation at + 1.5 V. XPS high resolution Si 2p spectra for SAMs* ***S–2*** *(j) freshly prepared, (k) after oxidation at + 0.6 V, and (l) after oxidation at + 1.5 V. FTIR spectra for silicon powder at freshly prepared and after oxidation at ambient conditions (21 °C and 30% relative humidity) for 30 days, m) Si–H, n) Si–D. Si–D stretching is clearly visible at 1420 cm^{-1}, also Si–D bending is clearly visible at 565 cm^{-1}. These signals become weaker after leaving the Si–D surfaces at ambient conditions for 30 days. Si–H stretching and bending are weak even in the fresh state.*

3.2. Fourier-transform infrared spectroscopy (FTIR)

FTIR experiments were performed on silicon powder obtained by grinding Si wafers. The silicon was grinded with a mortar and then etched using the same procedure used with the flat silicon wafers. Si–H powder starts with a significant amount of oxide, with Si–O stretching appearing at 714 cm^{-1} and Si–O–C stretching at 1077 cm^{-1}. Only small signals appear at 626 cm^{-1} and between 2000–2200 cm^{-1}, which are attributed to Si–H bending and stretching, respectively. On the other hand, on Si–D surfaces, Si–D stretching is clearly visible at 1420 cm^{-1}; also Si–D bending is clearly visible at 565 cm^{-1}. These signals become significantly weaker after leaving the Si–D surfaces at ambient conditions for 30 days. (Figure 2m, n). The signal at 885 cm^{-1} is related to SiD_2 scissors. Importantly the Si–D bending at 565 cm^{-1} is significantly closer (versus Si–H at 626 cm^{-1}) to the Si phonon modes (452 cm^{-1}). The proximity of the Si–D bending modes to the bulk Si phonons is expected to result in an efficient channel for de-excitation. Therefore, it is expected that Si–H surfaces will reach a highly excited vibrational state for a longer time compared to Si–D. Deuterium should therefore be much more difficult to be removed from the surface. This is especially the case if H or D desorption are involved in Si oxidation.

3.3. Electrochemical Studies

We first tested whether a typical hydrosilylation reaction with alkynes works equally on Si–D and on Si–H surfaces. While, the reaction was successful on both type of surfaces, the surface coverage was lower on Si–D surfaces when the reaction time of the hydrosilylation reaction was short (10 minutes). However, when the reaction was carried for 120 minutes, both Si–H and Si–D showed similar amount of surface coverages. The coverages were determined indirectly by attaching a ferrocene at the distal end after the hydrosilylation reaction by an azide-alkyne click reaction. (Figure S6, Table S2, Supporting Information). These results are an indication that the desorption of Si–D from the surface is slower than that of Si–H surfaces inferred by the higher surface coverages obtained on Si–D compared to Si–H surfaces. To compare the level of oxidation in the protonated and deuterated Si surfaces electrochemically under the influence of bias-voltages, we used similar type of surfaces, i.e. attaching a ferrocene moiety at the distal ends of the partially protonated (SAM **S–5**) and partially deuterated (SAM **S–6**). We then monitored the molecular surfaces coverages and the rate constant of electron transfer across the interface. When the Si oxidizes, it is expected the ferrocene terminated molecules will desorb for the surface leading to a decrease in the surface coverage and a lower charge transfer kinetics due to a reduced lateral electron transfer between neighboring ferrocene moieties.[39] First, we measured the nonadiyne surface coverage after applying + 0.6, + 1.0, + 1.5, – 0.6, – 1.0, and – 1.5 V. For this purpose, the potential was first applied to SAMs **S–3** and **S–4** for a specific amount of time. These surfaces are the partially protonated (**S–3)** and deuterated (**S–4)** nonadiyne terminated surfaces before any induced oxidation (See Figure 1). The resulting SAMs **S–5** and **S–6** were then reacted with azidomethylferrocene via an azide-alkyne "click" reaction yielding SAMs **S–7** and **S–8**. Figure 3 show the CVs for SAMs **S–7** and **S–8** after applying a potential of + 0.6, + 1.0, + 1.5, – 0.6 , – 1.0 , and – 1.5

V for 1 minute, 5 minutes, and 10 minutes on SAMs **S–5** and **S–6**. The CVs show the characteristic redox peaks of the ferrocene moiety at ~ 0.45 V vs Ag/AgCl (Figure S7, Supporting Information). The key observation from the CVs is the decrease in molecular coverage with the magnitude and duration of the applied potential but of different magnitude for the protonated and deuterated surfaces respectively. In all cases the Si–D surfaces performed better than Si–H surfaces in terms of oxidation both at negative and positive potentials. This is especially the case when the biases applied are moderate and when the Si surface is biased negatively (– 0.6, – 1V) and when applied for a shorter period of time (1, 5 minutes). For example, The surface coverage of SAM **S–8** decreases by ~ 2% from (1.65 ± 0.38) × 10^{14} ferrocene cm^{-2} in the fresh state to (1.62 ± 0.34) × 10^{14} ferrocene cm^{-2} when the potential of – 0.6 V applied for 1 minute on the partially deuterated SAM **S–6**. In contrast, the molecular coverage in SAM **S–7** decreases by ~ 31% from (1.89 ± 0.47) × 10^{14} ferrocene cm^{-2} in the fresh state to (1.31 ± 0.29) × 10^{14} ferrocene cm^{-2} when a potential of – 0.6 V was applied for 1 minute on the partially protonated coverage of SAM **S–8** decreases by ~ 40% from (1.65 ± 0.38) × 10^{14} ferrocene cm^{-2} in the fresh state to (9.87 ± 2.37) × 10^{13} ferrocene cm^{-2} when the potential of + 1.0 V applied for 5 minutes on partially deuterated

SAM **S–6**. In comparison, the molecular coverage in partially protonated SAM **S–7** decreases by ~ 50% from (1.89 ± 0.47) × 10^{14} ferrocene cm^{-2} in the fresh state to (9.32 ± 2.39) × 10^{13} ferrocene cm^{-2} when the potential of + 1.0 V was applied for 5 minutes on the partially H–terminated SAM **S–5**. This agrees with what we proposed in the introduction that the mechanism by which oxidation happens at positive and negative voltages are different. At negative voltages, the main contributor to the oxidation is desorption of the D and H from the surface. Because D is much more difficult to remove from the surface, the Si–D is significantly more resistant to oxidation at negative voltages.

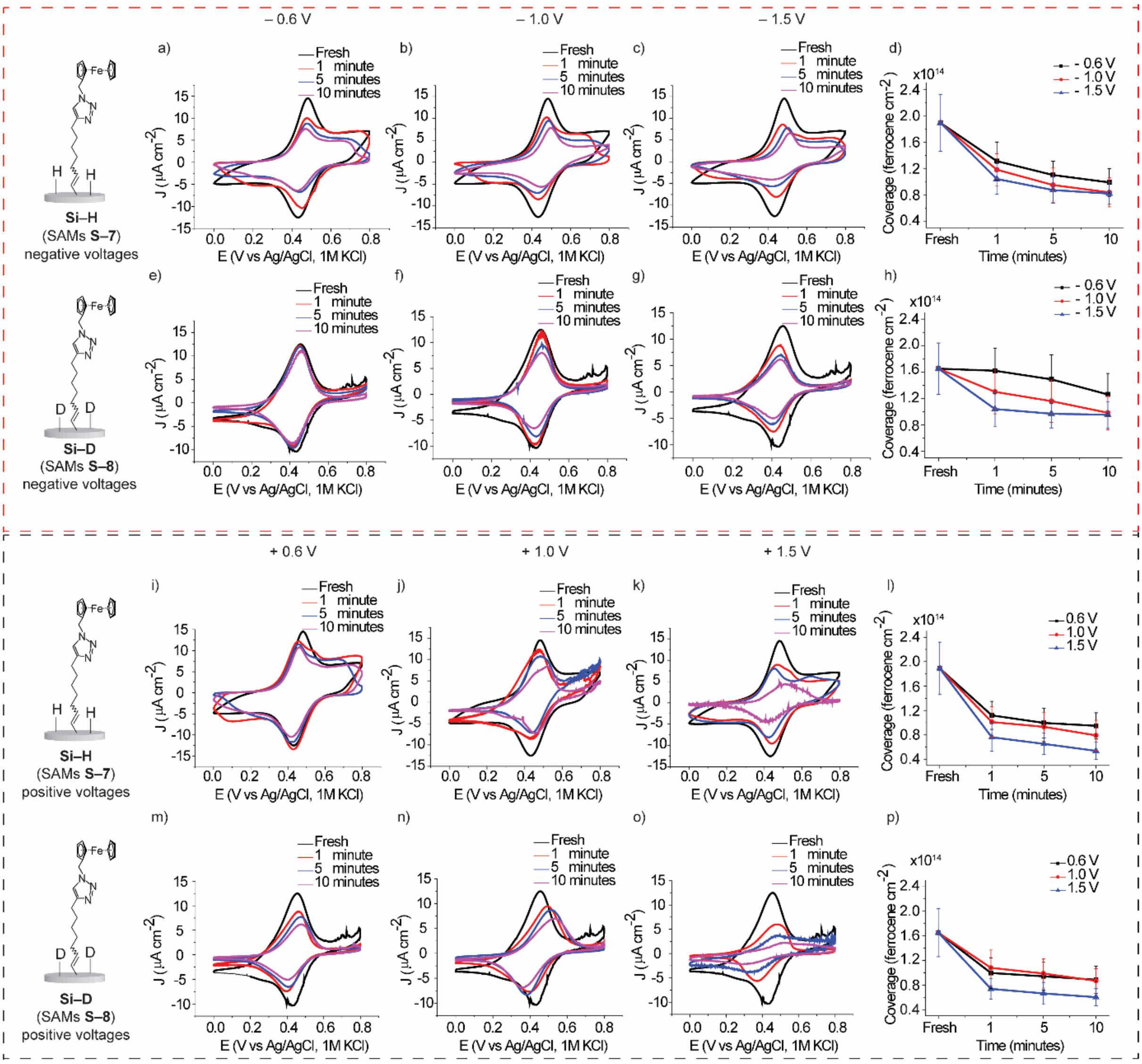

Figure 3. *Cyclic voltammetry for SAMs **S–7** which is obtained after applying to SAMs **S–5** an electrochemical potential of a) – 0.6 V, b) – 1.0 V and, c) – 1.5 V for 1, 5 and 10 minute, respectively. Cyclic voltammetry for SAMs **S–8** which is obtained after applying to SAMs **S–6** an electrochemical potential of e) – 0.6 V, f) – 1.0 V and, g) – 1.5 V for 1, 5 and 10 minute, respectively. Cyclic voltammetry for SAMs **S–7** which is obtained after applying to SAMs **S–5** an electrochemical potential of i) + 0.6 V, j) + 1.0 V and, k) +1.5 V for 1, 5 and 10 minutes, respectively. Cyclic voltammetry for SAMs **S–8** which is obtained after applying to SAMs **S–6** an electrochemical potential of m) + 0.6 V, n) + 1.0 V and, o) + 1.5 V for 1, 5 and 10 minutes, respectively. The corresponding surface coverages (d), (h), (l), and (p) are calculated from the oxidation waves of the CVs in (a), (b), (c), (e), (f), (g), (i), (j), (k), (m), (n), and (o). The error bars in (d), (h), (l), and (p) are the standard deviation of surface coverages from the mean value of three different surfaces. All CVs data were performed at the scan rate of 0.1 V/s.*

Table 1. The decrease in molecular coverages as a function of voltage and voltage duration applied for SAMs **S–7** and **S–8** compared with the fresh state (%).

Time **Voltage**	**1 minute**		**5 minutes**		**10 minutes**	
	Si–H (**S–7**)	Si–D (**S–8**)	Si–H (**S–7**)	Si–D (**S–8**)	Si–H (**S–7**)	Si–D (**S–8**)
– 0.6 V	31% ± 2%	2% ± 0.2%	42% ± 4%	10% ± 1%	48% ± 3%	24% ± 3%
– 1.0 V	38% ± 4%	21% ± 1%	50% ± 4%	30% ± 2%	56% ± 6%	40% ± 4%
– 1.5 V	45% ± 3%	37% ± 4%	54% ± 7%	41% ± 5%	57% ± 5%	42% ± 6%
+ 0.6 V	41% ± 5%	40% ± 3%	47% ± 5%	43% ± 2%	50% ± 5%	46% ± 5%
+ 1.0 V	38% ± 4%	35% ± 4%	50% ± 6%	40% ± 4%	58% ± 5%	47% ± 6%
+ 1.5 V	60% ± 6%	55% ± 4%	66% ± 8%	60% ± 5%	72% ± 7%	64% ± 5%

At positive voltages Si–D is also more resistant to oxidation then Si–H but because the oxidation is induced by the ability of the surface to attract OH^-, the difference is not as high.[60] The molecular coverage decrease rate are shown in the Table 1.

Another parameter used to monitor oxidation of the Si is measuring differences in the charge transfer kinetics as a function of the applied biases. Electrochemical impedance spectroscopy (EIS) was performed on SAMs **S–7** and **S–8**. (Figure 4) SAMs **S–7** and **S–8** served as the electrodes and 1 M perchloric acid served as the electrolyte. The Randles circuit used to fit the EIS data and the charge transfer resistance was extracted and the rate constant calculated (Figure S8, Supporting Information). It is expected that the rate constant of electron transfer will follow the decrease in surface coverage observed in section 3.3.

This is because decrease in surface coverage reduce lateral electron transfer between ferrocene moieties which in turn reduces the overall standard rate constant (k_{et}). The decrease in k_{et} followed the same trend observed for the decrease in molecular coverages as a function of the applied potentials. This is especially the case when the biases applied are moderate and when the Si surface is biased negatively (– 0.6, – 1V) and when applied for a shorter period of time (1, 5 minutes). For example, the rate constants (k_{et}) of SAM **S–8** decreases by 18% from (21.37 ± 0.92) s^{-1} in the fresh state to (17.43 ± 0.64) s^{-1} when the potential of – 0.6 V was applied for 1 minute on SAM **S–6**. In comparison, SAM **S–7** decreases by 27% from (170.76 ± 6.29) s^{-1} in the fresh state to (124.97 ± 12.19) s^{-1} when the potential of – 0.6 V applied for 1 minute on SAM **S–5**. When higher biases are applied for longer time, the SAM **S–5**. Similar trend was observed at positive voltages but the differences is smaller. The surface protonated and deuterated version of the surfaces show approximately equal oxidation. Details are provided in Table 2.

3.4. Conducting AFM studies

After performing the wet electrochemical experiments, C–AFM was used to test how a bias–voltage applied between a Pt AFM tip and the Si–D surface (SAM **S–2**, Figure 5f–j) affects current–voltage measurements typically used in semiconductor measurements. These experiments differ from the electrochemical experiments (section 3.3) in that they are performed in dry conditions without an electrochemical control. The bias voltage between the tip and the surface was applied to SAM **S–2** at specific location for 8 minutes. Topography images were then recorded at low bias–voltages to check what the effect of the previous bias–voltage applied was (Figure 5a–e). On Si–H surfaces[48], it was previously demonstrated that the oxide thickness increased with the magnitude of the bias–voltage applied from (1.0 ± 0.36) nm to (6.3 ± 0.37) nm as the bias-voltage increased from + 0.5 V to + 5 V. Also on Si–H the oxide square created in the center of the surface becomes clearly visible at + 0.5 V. In contrast, Si–D surfaces the oxide square does not reach detectable thickness until + 5 V. In addition, I–V measurements were performed on and outside the oxide areas. When the bias-voltage applied exceeded +

0.5 V, the resulting oxide growth affected the magnitude of the current compared to that recorded on unbiased surfaces (Figure 5k–o). On the Si–D surfaces, the I–V curves changed from a typical rectifying metal–semiconductor junction to nearly an insulator for applied potentials beyond + 5 V, however, on the Si–H surfaces, switching to the insulating state that completely blocks the current occurred at a lower bias voltage of + 3 V. Also on Si–H surfaces, the I–V curves deviate from their initial state (on surfaces before applying the voltages) on surfaces that was exposed to a bias as little as + 0.5 V. However on Si–D surfaces the I–V characteristics remains stable up to + 3V.

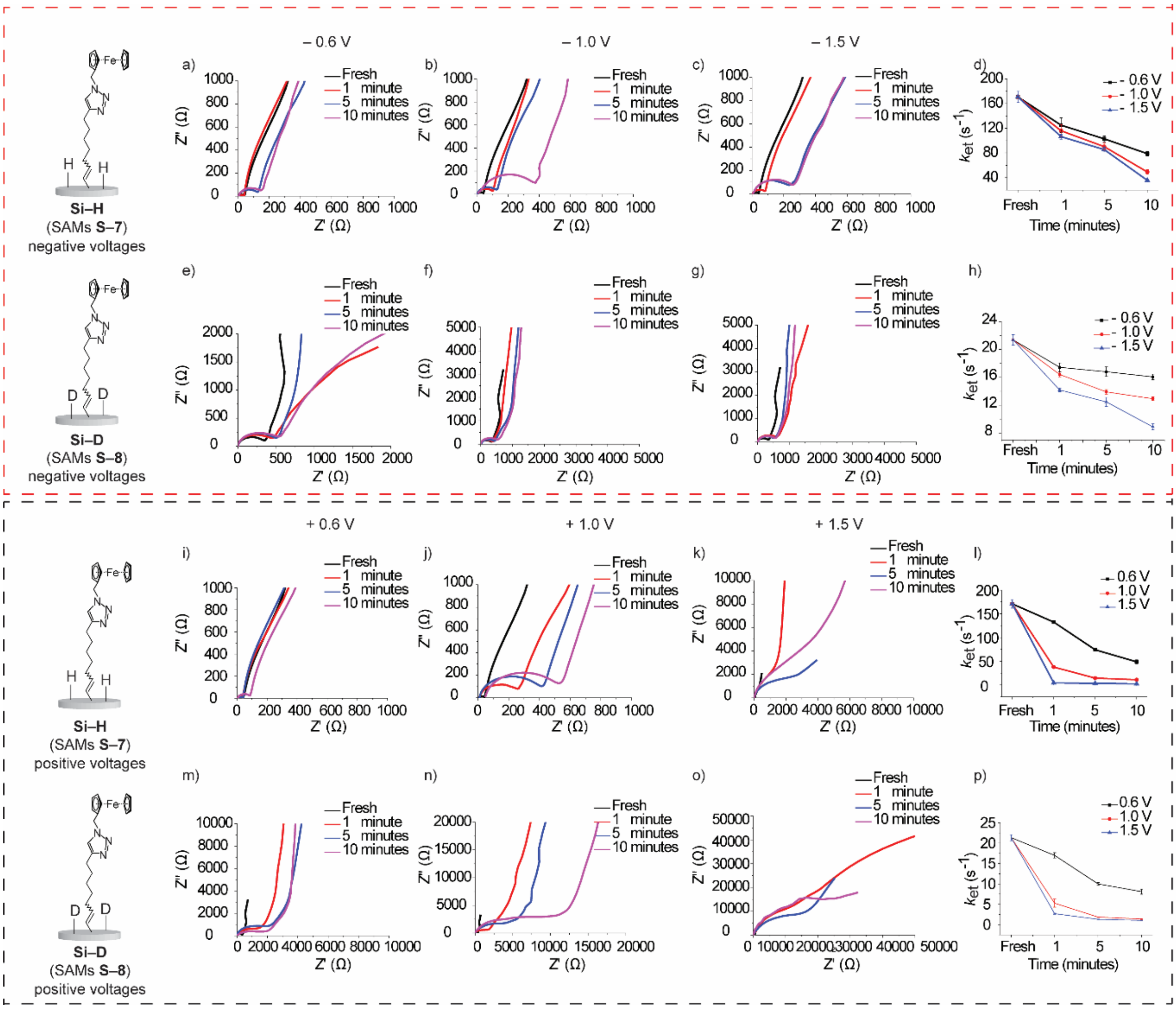

Figure 4. *Nyquist plots from EIS measurements of SAMs* ***S–7*** *which is obtained after applying to SAMs* ***S–5*** *an electrochemical potential of a) – 0.6 V, b) – 1.0 V and, c) – 1.5 V for 1, 5 and 10 minutes, respectively. Nyquist plots from EIS measurements of SAMs* ***S–8*** *which is obtained after applying to SAMs* ***S–6*** *an electrochemical potential of e) – 0.6 V, f) – 1.0 V and, g) – 1.5 V for 1, 5 and 10 minutes, respectively. Nyquist plots from EIS measurements of SAMs* ***S–7*** *which is obtained after applying to SAMs* ***S–5*** *an electrochemical potential of i) + 0.6 V, j) + 1.0 V and, k) + 1.5 V for 1, 5 and 10 minutes, respectively. Nyquist plots from EIS measurements of SAMs* ***S–8*** *which is obtained after applying to SAMs* ***S–6*** *an electrochemical potential of m) + 0.6 V, n) + 1.0 V and, o) + 1.5 V for 1, 5 and 10 minutes, respectively. The corresponding evolution in* k_{et} *(d), (h), (l), and (p) are calculated from the oxidation waves of the CVs in (a), (b), (c), (e), (f), (g), (i), (j), (k), (m), (n), and (o). The error bars in (d), (h), (l), and (p) is the standard deviation of* k_{et} *from the mean value of three different surfaces. All fitting data were shown in the Table S3-S15 (Supporting Information).*

Table 2. The decrease in k_{et} for SAMs **S–7** and **S–8** as a function of voltage and voltage duration applied compared to a freshly prepared surface (%).

Time / **Voltage**	**1 minute**		**5 minutes**		**10 minutes**	
	Si–H (**S–7**)	Si–D (**S–8**)	Si–H (**S–7**)	Si–D (**S–8**)	Si–H (**S–7**)	Si–D (**S–8**)
– 0.6 V	27% ± 4%	18% ± 2%	40% ± 5%	21% ± 2%	54% ± 5%	25% ± 3%
– 1.0 V	32% ± 3%	23% ± 2%	47% ± 4%	35% ± 3%	71% ± 6%	40% ± 3%
– 1.5 V	38% ± 5%	34% ± 4%	50% ± 7%	42% ± 4%	79% ± 7%	58% ± 5%
+ 0.6 V	22% ± 3%	20% ± 2%	56% ± 6%	53% ± 4%	71% ± 7%	62% ± 5%
+ 1.0 V	78% ± 7%	75% ± 7%	92% ± 3%	91% ± 4%	94% ± 5%	93% ± 4%
+ 1.5 V	97% ± 2%	87% ± 4%	98% ± 2%	95% ± 3%	99% ± 0.5%	96% ± 2%

4. DISCUSSION

The electrochemical and electrical measurements above indicate that Si–D is more resistant to oxidation than Si–H in both the electrochemical and the C–AFM studies. In the electrochemical experiments, the Si–D was more resistant to oxidation especially at negative voltages. For example in the XPS, when the bias voltage applied was – 0.6 V for 1 minute, the oxide content on Si–D was not detectable compared to 20.7% on Si–H. This is consistent with what was observed in the electrochemical measurements, which showed when the bias-voltage applied was – 0.6 V for 1 minute, the molecular coverage decreased 2% on Si–D surfaces, however, a decrease of 31% was observed for Si–H surfaces. In the C–AFM experiments, the oxide thickness increases from 0 nm to (6.3 ± 0.37) nm when the bias-voltage increase from 0 V to + 5 V on Si–H surfaces. At higher voltages of ± 1.5 V, the differences between Si–H and Si–D become very small. At negative potential/biases, there is in stark contrast to Si–D surfaces that resisted any oxidation up until 5 V. Si–H bonds are expected to reach a highly excited vibrational state for a longer time as compared to Si–D, and therefore, Si–D is expected to better resist cleavage than Si–H [61]. These vibrational properties of the bond likely explain the reason why Si–D is more stable and more resistant to oxidation than Si–H when the Si is biased negatively. At positive potential and biases, however, oxidation of silicon is usually dominated by the attraction of OH^- from the solution in the electrochemical measurements or from water adsorption on the surface in C–AFM studies[62]. This interpretation is consistent with the differences in the work functions of Si–H versus Si–D surfaces determined by UV photoelectron spectroscopy (UPS), which revealed a work function of 4.92 eV for Si–H surfaces and 5.33 eV for Si–D surfaces, respectively, indicating that it requires more energy for the Si–D to become positively charged and consequently attract OH^- ions. To further investigate whether the adsorption of OH^- on Si–H is different than Si–D, the flat band potential of each surface was determined. SAMs **S–1** and **S–2** served as the electrodes and 1 mM tetrabutylammonium hexafluorophosphate dissolved in 10 mL of acetonitrile served as the electrolyte. Figure 6c, d show Mott-Schottky plot via which the flat band potential for **S–1** and **S–2** surfaces were determined. It is expected that the further the applied potential from flat band potential is for each surface, the more capable is the surface in attracting OH^-. At the applied voltage range of + 0.6–1.5 V, Si–H surfaces will be comparably more positively than Si–D (flat band potential of Si–H is 130 mV more negative than Si–D surfaces). The greater ability of the OH^- to adsorb on the Si–H surfaces makes it more prone to oxidation as compared to Si–D at positive voltages.

To investigate the effect of dissolved oxygen on the oxidation process, we performed the experiment (applying electrochemical potentials) after saturating the solution with bubbled oxygen.

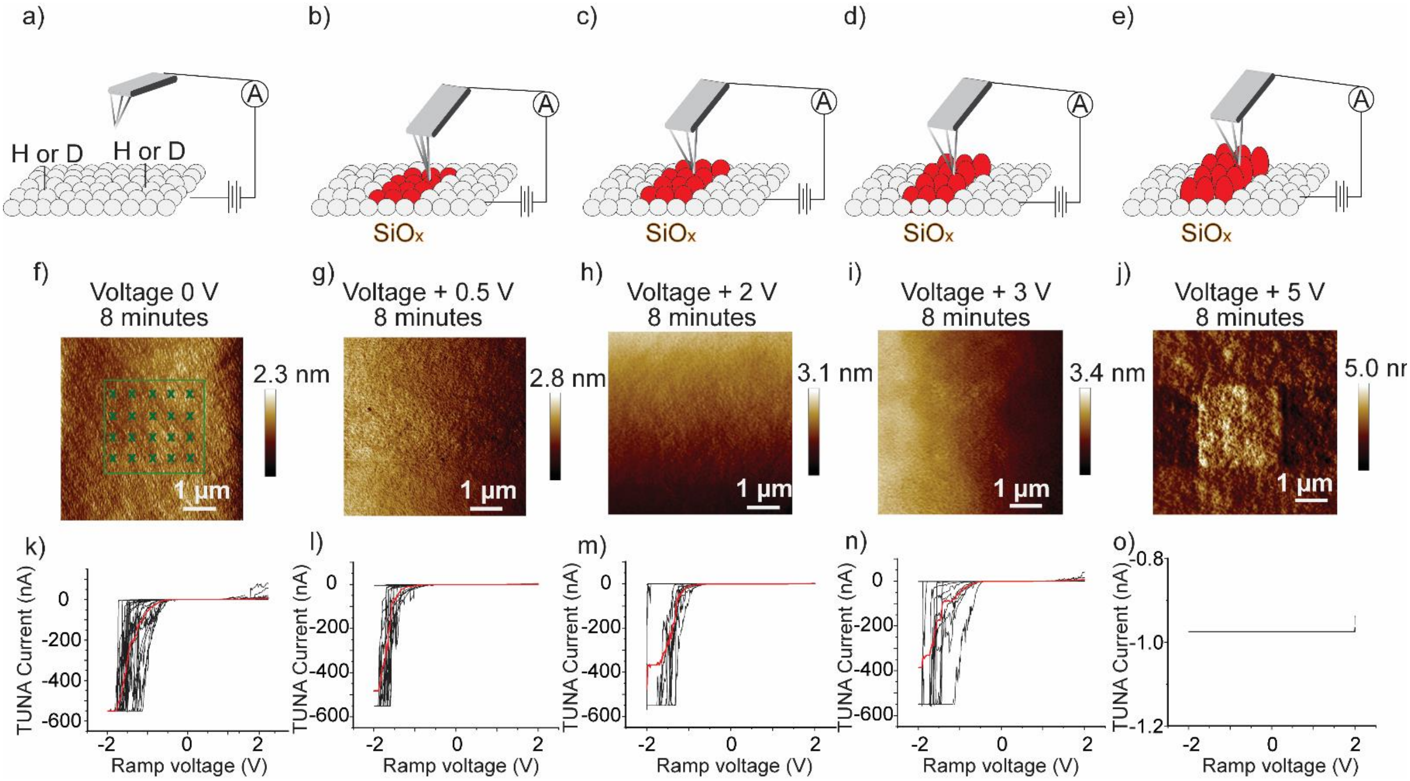

Figure 5. *(a–e) Cartoons describing the respective experiments and each surface. AFM topography of the oxide squares obtained on SAM* ***S–2*** *by AFM–tip induced oxidation at no bias–voltage (0 V) (f), + 0.5 V (g), + 2 V (h), + 3 V (i) and + 5 V (j) for 8 minutes. I–V curves of the* ***S–1*** *biased at 0 V (k), + 0.5 V (l), + 2 V (m), + 3 V (n), + 5 V (o). The red line in Figure (k–o) is the average TUNA current for 20 curves. Positive bias means the Si is positively biased relative to the tip. The data for Si–H is from Ref. 68.*[48]

The results show that for SAMs **S–8**, the coverage decrease less from (1.65 ± 0.38) × 10^{14} ferrocene cm^{-2} to (1.09 ± 0.29) × 10^{14} ferrocene cm^{-2} after oxygen gas was bubbled at + 1 V for 5 minutes. On the other hand, the coverage of SAMs **S–8** decrease from (1.65 ± 0.38) × 10^{14} ferrocene cm^{-2} to (8.79 ± 2.29) × 10^{13} ferrocene cm^{-2} after oxygen gas was bubbled at –1 V for 5 minutes. (Figure S9, Supporting Information) Therefore, it appears that the presence of dissolved O_2 affect the oxide layer formation more significantly at negative voltages, while it appears that at positive voltages the major contribution to oxidation is the OH^- ions.

Finally, we have performed time-resolved photocurrent mapping which revealed a recombination time constant of (44.3 ± 15.7) µs and (51.8 ± 19.6) µs for Si–D and Si–H surfaces, respectively. The comparable decay indicates that Si–D has similar surface defects of typical Si–H surfaces.

5. CONCLUSIONS

In summary, we demonstrated that when H is replaced with D, Si oxidation is significantly inhibited when subjected to high electric fields. Whether it is in macroscale electrochemical experiments or nanoscale current–voltage measurements, Si–D surfaces perform significantly better than Si–H surfaces. We therefore recommend changing the typical procedures used in etching Si and endorse Si–D surfaces instead of Si–H surfaces for applications requiring non-oxidized Si surfaces. This recommendation is applicable for electrochemical biosensors based on Si which utilizes electrochemical signals[63, 64], Si-based molecular electronics devices[65-67], and Si-based triboelectric generators[68].

The strong isotope effect is interpreted by the frequency of the bending modes of Si–D being closer to that of the bulk Si surface phonons than Si–H. It is therefore expected that Si–D can be de-excited rapidly via the Si phonon modes. This can lead to surface bound Si–D bonds being much more resistant to desorption than Si–H, which in turn, can limit homolytic cleavage and the generation of Si radicals that initiate Si oxidation when the Si surface is negatively biased. At positive voltages, Si–D surfaces appears less attractive to oxidizing OH$^-$ ions because Si–D have a more positive flat band potential compared to that of Si–H surfaces. The strong surface isotope effects reported here have implication in the design of silicon-based devices, molecular electronics and power-generation devices based on silicon, and on the interpretation of their charge transport characteristics.

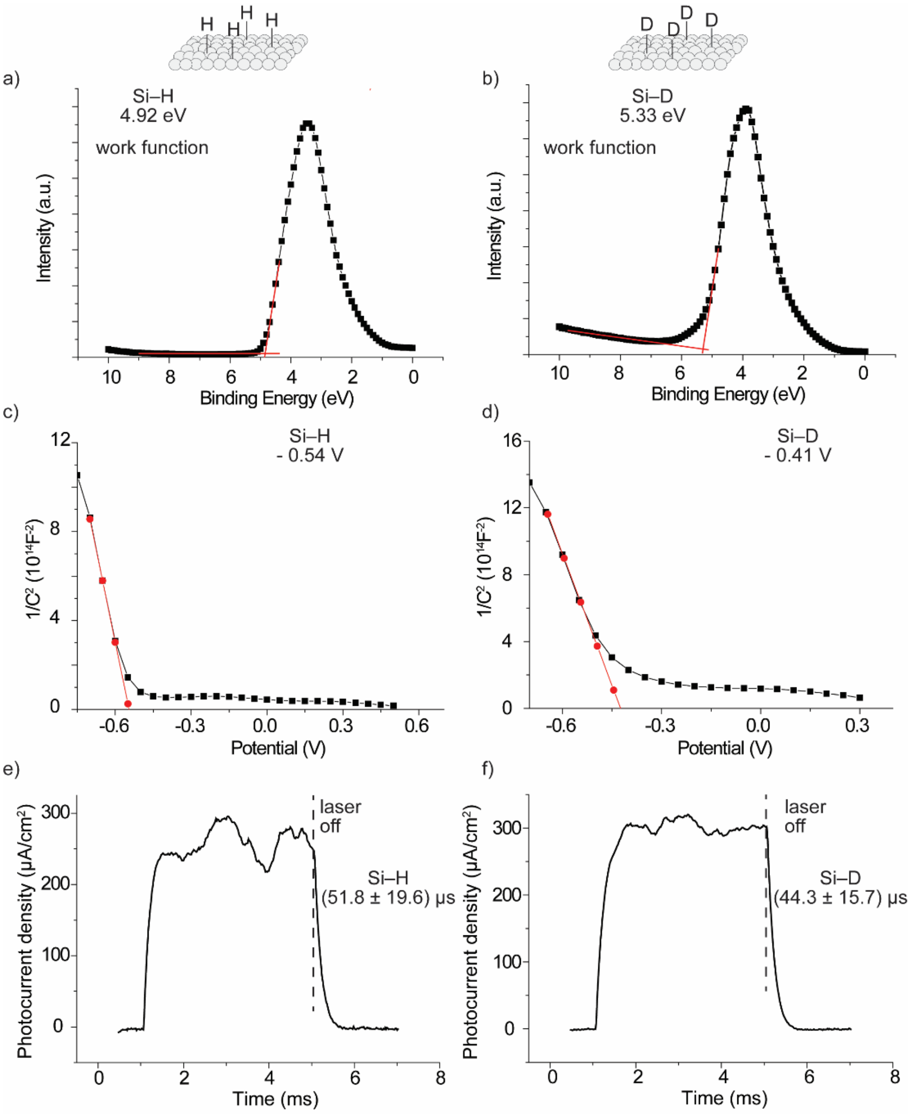

Figure 6. *UPS spectra of the secondary edge region of a) Si–H surface (4.92 eV), b) Si–D surface (5.33 eV). The black line is the acquired data and the red lines are linear fits to the flat and steep regions. The work function was estimated from the position of the intersection between the flat lines. The x-axis binding energy has been corrected to account for the excitation energy (21.22 eV). Mott-Schottky plot of c) Si–H surface, d) Si–D surface and flat band potential fitting for each surfaces. The black line is the acquired data and the red lines are linear fitting. The flat band potential is the intersection point of linear fitting and x-axis. (e–f) Transient microscopic* photocurrent map *measurements (PCM) on static silicon–platinum junctions. Representative photocurrent decay curves measured on e) Si–H surface, f) Si–D surface. The time constant calculated from the non-linear fitting with exponential category and function of* $y = y_0 + A \bullet e^{Ro \bullet x_1}$.

SUPPORTING INFORMATION

Detailed contact angle, XPS and electrochemical analysis are supplied as Supporting Information.

AUTHOR CONTRIBUTIONS

N.D. conceived the idea and supervised the research. T. Li performed the electrochemical measurements, IR and water-contact angle measurements and assisted in the C-AFM measurements. C. Peiris performed the AFM measurements. M. MacGregor performed the XPS and UPS measurements. C. Hurtado helped in performing the time-resolved photocurrent mapping experiments. All authors contributed to the interpretation of the data. N.D. and T.Li wrote the manuscript.

NOTES

The authors declare no competing financial interest.

FUNDING SOURCES

The authors acknowledge support from the Australian Research Council (DP190100735, FT200100301). The National Deuteration Facility is partly supported by the National Collaborative Research Infrastructure Strategy (NCRIS) an initiative of the Australian Government. MM acknowledge the instruments and expertise of Microscopy Australia enabled by NCRIS, university, and state government support. AK is a Rothwell Family Fellow.

6. REFERENCES

1. Lyding, J. W.; Hess, K.; Kizilyalli, I. C., Reduction of Hot Electron Degradation in Metal Oxide Semiconductor Transistors by Deuterium Processing. *Appl. Phys. Lett.* **1996,** *68* (18), 2526-2528.
2. Tang, W. S.; Dimitrievska, M.; Chotard, J.-N. l.; Zhou, W.; Janot, R. l.; Skripov, A. V.; Udovic, T. J., Structural and Dynamical Trends in Alkali-metal Silanides Characterized by Neutron-scattering Methods. *J. Phys. Chem. C* **2016,** *120* (38), 21218-21227.
3. Yang, T.; Thomas, A. M.; Dangi, B. B.; Kaiser, R. I.; Mebel, A. M.; Millar, T. J., Directed Gas Phase Formation of Silicon Dioxide and Implications for the Formation of Interstellar Silicates. *Nat. Commun.* **2018,** *9* (1), 1-8.
4. Guyot-Sionnest, P.; Lin, P.; Hiller, E., Vibrational Dynamics of the Si–H Stretching Modes of the Si (100)/H: 2× 1 Surface. *Chem. Phys.* **1995,** *102* (10), 4269-4278.
5. Avouris, P.; Walkup, R.; Rossi, A.; Shen, T.-C.; Abeln, G.; Tucker, J.; Lyding, J., STM-induced H Atom Desorption from Si (100): Isotope Effects and Site Selectivity. *Chem. Phys. Lett.* **1996,** *257* (1-2), 148-154.
6. Li, Y.; Calder, S.; Yaffe, O.; Cahen, D.; Haick, H.; Kronik, L.; Zuilhof, H., Hybrids of Organic Molecules and Flat, Oxide-free Silicon: High-density Monolayers, Electronic Properties, and Functionalization. *Langmuir* **2012,** *28* (26), 9920-9929.
7. de Smet, L. C.; Zuilhof, H.; Sudhölter, E. J.; Lie, L. H.; Houlton, A.; Horrocks, B. R., Mechanism of the Hydrosilylation Reaction of Alkenes at Porous Silicon: Experimental and Computational Deuterium Labeling Studies. *J. Phys. Chem. B* **2005,** *109* (24), 12020-12031.
8. Luo, H.; Chidsey, C. E. D.; Chabal, Y., Infrared Spectroscopy of Covalently Bonded Species on Silicon Surfaces: Deuterium, Chlorine, and Cobalt Tetracarbonyl. *MRS Proceedings* **1997,** *477*, 415.
9. Guengerich, F. P., Kinetic Deuterium Isotope Effects in Cytochrome P450 Reactions. In *Meth. Enzymol.*, Elsevier: 2017; Vol. 596, pp 217-238.
10. Bonanos, N.; Huijser, A.; Poulsen, F. W., H/D Isotope Effects in High Temperature Proton Conductors. *Solid State Ion.* **2015,** *275*, 9-13.
11. Buijs, J.; Ramström, M.; Danfelter, M.; Larsericsdotter, H.; Håkansson, P.; Oscarsson, S., Localized Changes in the Structural Stability of Myoglobin Upon Adsorption onto Silica Particles, as Studied with Hydrogen/Deuterium Exchange Mass Spectrometry. *J. Colloid Interface Sci.* **2003,** *263* (2), 441-448.
12. Yu, G.; Zhou, Y.; Yang, R.; Wang, M.; Shen, L.; Li, Y.; Xue, N.; Guo, X.; Ding, W.; Peng, L., Dehydration and Dehydroxylation of Layered Double Hydroxides: New Insights from Solid-state NMR and FT-IR Studies of Deuterated Samples. *J. Phys. Chem. C* **2015,** *119* (22), 12325-12334.
13. Shen, T.-C.; Wang, C.; Abeln, G.; Tucker, J.; Lyding, J.; Avouris, P.; Walkup, R., Atomic-Scale Desorption through Electronic and Vibrational Excitation Mechanisms. *Science* **1995,** *268* (5217),

1590-1592.

14. Tuttle, B.; Van de Walle, C. G., Structure, Energetics, and Vibrational Properties of Si-H Bond Dissociation in Silicon. *Phys. Rev. B* **1999,** *59* (20), 12884.

15. Li, T.; Dief, E. M.; Kalužná, Z.; MacGregor, M.; Foroutan-Nejad, C.; Darwish, N., On-Surface Azide–Alkyne Cycloaddition Reaction: Does It Click with Ruthenium Catalysts? *Langmuir* **2022,** *38* (18), 5532-5541.

16. Sam, S.; Touahir, L.; Salvador Andresa, J.; Allongue, P.; Chazalviel, J.-N.; Gouget-Laemmel, A.; Henry de Villeneuve, C.; Moraillon, A.; Ozanam, F.; Gabouze, N., Semiquantitative Study of the EDC/NHS Activation of Acid terminal Groups at Modified Porous Silicon Surfaces. *Langmuir* **2010,** *26* (2), 809-814.

17. Peiris, C. R.; Ciampi, S.; Dief, E. M.; Zhang, J.; Canfield, P. J.; Le Brun, A. P.; Kosov, D. S.; Reimers, J. R.; Darwish, N., Spontaneous S–Si Bonding of Alkanethiols to Si (111)–H: Towards Si–Molecule–Si Circuits. *Chem. Sci.* **2020,** *11* (20), 5246-5256.

18. Vogel, Y. B.; Gonçales, V. R.; Al-Obaidi, L.; Gooding, J. J.; Darwish, N.; Ciampi, S., Nanocrystal Inks: Photoelectrochemical Printing of Cu2O Nanocrystals on Silicon with 2D Control on Polyhedral Shapes. *Adv. Funct. Mater.* **2018,** *28* (51), 1804791.

19. Yokoyama, Y.; Ishiguro, R.; Maeda, H.; Mukaiyama, M.; Kameyama, K.; Hiramatsu, K., Quantitative Analysis of Protein Adsorption on a Planar Surface by Fourier Transform Infrared Spectroscopy: lysozyme Adsorbed on Hydrophobic Silicon-Containing Polymer. *J. Colloid Interface Sci.* **2003,** *268* (1), 23-32.

20. Aragonès, A. C.; Darwish, N.; Ciampi, S.; Sanz, F.; Gooding, J. J.; Díez-Pérez, I., Single-Molecule Electrical Contacts on Silicon Electrodes under Ambient Conditions. *Nat. Commun.* **2017,** *8* (1), 1-8.

21. De Villeneuve, C. H.; Pinson, J.; Bernard, M.; Allongue, P., Electrochemical Formation of Close-packed Phenyl Layers on Si (111). *J. Phys. Chem. B* **1997,** *101* (14), 2415-2420.

22. Chen, H.; Jiang, F.; Hu, C.; Jiao, Y.; Chen, S.; Qiu, Y.; Zhou, P.; Zhang, L.; Cai, K.; Song, B., Electron-Catalyzed Dehydrogenation in a Single-Molecule Junction. *J. Am. Chem. Soc.* **2021,** *143* (22), 8476-8487.

23. Darwish, N.; Díez-Pérez, I.; Da Silva, P.; Tao, N.; Gooding, J. J.; Paddon-Row, M. N., Observation of Electrochemically Controlled Quantum Interference in a Single Anthraquinone-based Norbornylogous Bridge Molecule. *Angew. Chem., Int. Ed. Engl.* **2012,** *51* (13), 3203-3206.

24. Cohen, Y. S.; Vilan, A.; Ron, I.; Cahen, D., Hydrolysis Improves Packing Density of Bromine-Terminated Alkyl-Chain, Silicon− Carbon Monolayers Linked to Silicon. *J. Phys. Chem. C* **2009,** *113* (15), 6174-6181.

25. Gooding, J. J.; Darwish, N., The Rise of Self-assembled Monolayers for Fabricating Electrochemical Biosensors—An Interfacial Perspective. *Chem. Rec.* **2012,** *12* (1), 92-105.

26. Touahir, L.; Allongue, P.; Aureau, D.; Boukherroub, R.; Chazalviel, J.-N.; Galopin, E.; Gouget-Laemmel, A.; de Villeneuve, C. H.; Moraillon, A.; Niedziółka-Jönsson, J., Molecular Monolayers on Silicon as Substrates for Biosensors. *Bioelectrochemistry* **2010,** *80* (1), 17-25.

27. Rahpeima, S.; Le Brun, A.; Raston, C. L.; Darwish, N., Electro-polymerization rates of diazonium salts are dependent on the crystal orientation of the surface. *J. Colloid Interface Sci.* **2022,** *626*, 985-994.

28. van Geenen, F. A.; Claassen, F. W.; Franssen, M. C.; Zuilhof, H.; Nielen, M. W., Laser Ablation Electrospray Ionization Hydrogen/Deuterium Exchange Ambient Mass Spectrometry Imaging. *J. Am. Soc. Mass Spectrom.* **2020,** *31* (2), 249-256.

29. Darwish, N.; Aragones, A. C.; Darwish, T.; Ciampi, S.; Diez-Perez, I., Multi-Responsive Photo- and Chemo-Electrical Single-Molecule Switches. *Nano Lett.* **2014,** *14* (12), 7064-7070.

30. Fabre, B.; Bassani, D. M.; Liang, C.-K.; Lhenry, S.; Hapiot, P., Photodimerization and Micropatterning of Anthracene-Appended Receptors Covalently Bound to Silicon Surfaces: En Route to Write–Read–Erase Molecular Print Board. *J. Phys. Chem. C* **2013,** *117* (24), 12725-12734.

31. Fabre, B.; Falaise, C. m.; Cadot, E., Polyoxometalates-Functionalized Electrodes for (Photo) Electrocatalytic Applications: Recent Advances and Prospects. *ACS Catal.* **2022,** *12*, 12055-12091.

32. van Andel, E.; Roosjen, M.; van der Zanden, S.; Lange, S. C.; Weijers, D.; Smulders, M. M. J.; Savelkoul, H. F. J.; Zuilhof, H.; Tijhaar, E. J., Highly Specific Protein Identification by

Immunoprecipitation–Mass Spectrometry Using Antifouling Microbeads. *ACS Appl. Mater. Interfaces* **2022,** *14* (20), 23102-23116.

33. Amdouni, S.; Cherifi, Y.; Coffinier, Y.; Addad, A.; Zaïbi, M. A.; Oueslati, M.; Boukherroub, R., Gold Nanoparticles Coated Silicon Nanowires for Efficient Catalytic and Photocatalytic Applications. *Mater. Sci. Semicond. Process* **2018,** *75*, 206-213.

34. Ferrie, S.; Darwish, N.; Gooding, J. J.; Ciampi, S., Harnessing Silicon Facet-dependent Conductivity to Enhance the Direct-current Produced by a Sliding Schottky Diode Triboelectric Nanogenerator. *Nano Energy* **2020,** *78*, 105210.

35. Darwish, N.; Foroutan-Nejad, C.; Domulevicz, L.; Hihath, J.; Díez-Pérez, I., Principles of Molecular Devices Operated by Electric Fields. In *Effects of Electric Fields on Structure and Reactivity*, 2021; pp 147-194.

36. Ma, L.; Lee, S.; DeMuth, J.; Maldonado, S., Direct Electrochemical Deposition of Crystalline Silicon Nanowires at T≥ 60° C. *RSC Adv.* **2016,** *6* (82), 78818-78825.

37. Jin, H.; Kinser, C. R.; Bertin, P. A.; Kramer, D. E.; Libera, J. A.; Hersam, M. C.; Nguyen, S. T.; Bedzyk, M. J., X-ray Studies of Self-assembled Organic Monolayers Grown on Hydrogen-terminated Si (111). *Langmuir* **2004,** *20* (15), 6252-6258.

38. Sun, Q. Y.; de Smet, L. C.; van Lagen, B.; Wright, A.; Zuilhof, H.; Sudhölter, E. J., Covalently Attached Monolayers on Hydrogen-Terminated Si (100): Extremely Mild Attachment by Visible Light. *Angew. Chem.* **2004,** *116* (11), 1376-1379.

39. Li, T.; Peiris, C.; Dief, E. M.; MacGregor, M.; Ciampi, S.; Darwish, N., Effect of Electric Fields on Silicon-Based Monolayers. *Langmuir* **2022,** *38* (9), 2986-2992.

40. Li, T.; Dief, E. M.; Lyu, X.; Rahpeima, S.; Ciampi, S.; Darwish, N., Nanoscale Silicon Oxide Reduces Electron Transfer Kinetics of Surface-Bound Ferrocene Monolayers on Silicon. *J. Phys. Chem. C* **2021,** *125* (50), 27763-27770.

41. Yuan, S.; Zhang, H.; Yuan, S., Reactive Molecular Dynamics on the Oxidation of Passivated H-terminated Si (111) Surface: 1-Alkynes vs 1-Alkenes. *Colloids Surf. A Physicochem. Eng. Asp.* **2020,** *606*, 125372.

42. Sieval, A. B.; Opitz, R.; Maas, H. P.; Schoeman, M. G.; Meijer, G.; Vergeldt, F. J.; Zuilhof, H.; Sudhölter, E. J., Monolayers of 1-Alkynes on the H-terminated Si (100) Surface. *Langmuir* **2000,** *16* (26), 10359-10368.

43. Rahpeima, S.; Dief, E. M.; Peiris, C. R.; Ferrie, S.; Duan, A.; Ciampi, S.; Raston, C. L.; Darwish, N., Reduced Graphene Oxide–Silicon Interface Involving Direct Si–O Bonding as A Conductive and Mechanical Stable Ohmic Contact. *ChemComm* **2020,** *56* (46), 6209-6212.

44. Rosso, M.; Giesbers, M.; Arafat, A.; Schroën, K.; Zuilhof, H., Covalently Attached Organic Monolayers on SiC and Si x N4 Surfaces: Formation Using UV Light at Room Temperature. *Langmuir* **2009,** *25* (4), 2172-2180.

45. Allongue, P.; de Villeneuve, C. H.; Cherouvrier, G.; Cortes, R.; Bernard, M.-C., Phenyl Layers on H–Si (111) by Electrochemical Reduction of Diazonium Salts: Monolayer versus Multilayer Formation. *J. Electroanal. Chem.* **2003,** *550*, 161-174.

46. Fabre, B.; Pujari, S. P.; Scheres, L.; Zuilhof, H., Micropatterned Ferrocenyl Monolayers Covalently Bound to Hydrogen-terminated Silicon Surfaces: Effects of Pattern Size on the Cyclic Voltammetry and Capacitance Characteristics. *Langmuir* **2014,** *30* (24), 7235-7243.

47. Seitz, O.; Vilan, A.; Cohen, H.; Hwang, J.; Haeming, M.; Schoell, A.; Umbach, E.; Kahn, A.; Cahen, D., Doping Molecular Monolayers: Effects on Electrical Transport through Alkyl Chains on Silicon. *Adv. Funct. Mater.* **2008,** *18* (14), 2102-2113.

48. Peiris, C. R.; Ferrie, S.; Ciampi, S.; Rickard, W. D.; Darwish, N., Memristor Arrays Formed by Reversible Formation and Breakdown of Nanoscale Silica Layers on Si–H Surfaces. *ACS Appl. Nano Mater.* **2022,** *5* (5), 6609-6617.

49. Rahpeima, S.; Dief, E. M.; Ciampi, S.; Raston, C. L.; Darwish, N., Impermeable Graphene Oxide Protects Silicon from Oxidation. *ACS Appl. Mater. Interfaces* **2021,** *13* (32), 38799-38807.

50. Luo, H.; Chidsey, C. E., D–Si (111)(1× 1) Surface for the Study of Silicon Etching in Aqueous Solutions. *Appl. Phys. Lett.* **1998,** *72* (4), 477-479.

51. Luo, H.; Chidsey, C. E.; Chabal, Y., Infrared Spectroscopy of Covalently Bonded Species on Silicon Surfaces: Deuterium, Chlorine, and Cobalt Tetracarbonyl. *Mater. Res. Soc. Symp. Proc.* **1997,** *477*, 415.

52. Oura, K.; Lifshits, V.; Saranin, A.; Zotov, A.; Katayama, M., Hydrogen Interaction with Clean and Modified Sicon Surfaces. *Surf. Sci. Rep.* **1999,** *35* (1-2), 1-69.

53. Turowski, M.; Yamakawa, N.; Meller, J.;

Kimata, K.; Ikegami, T.; Hosoya, K.; Tanaka, N.; Thornton, E. R., Deuterium Isotope Effects on Hydrophobic Interactions: the Importance of Dispersion Interactions in the Hydrophobic Phase. *J. Am. Chem. Soc.* **2003,** *125* (45), 13836-13849.

54. Ciampi, S.; Eggers, P. K.; Le Saux, G.; James, M.; Harper, J. B.; Gooding, J. J., Silicon (100) Electrodes Resistant to Oxidation in Aqueous Solutions: An Unexpected Benefit of Surface Acetylene Moieties. *Langmuir* **2009,** *25* (4), 2530-2539.

55. Ciampi, S.; Böcking, T.; Kilian, K. A.; James, M.; Harper, J. B.; Gooding, J. J., Functionalization of Acetylene-terminated Monolayers on Si (100) Surfaces: A Click Chemistry Approach. *Langmuir* **2007,** *23* (18), 9320-9329.

56. Jakša, G.; Štefane, B.; Kovač, J., XPS and AFM Characterization of Aminosilanes with Different Numbers of Bonding Sites on A Silicon Wafer. *Surf. Interface Anal.* **2013,** *45* (11-12), 1709-1713.

57. Jensen, D. S.; Kanyal, S. S.; Madaan, N.; Vail, M. A.; Dadson, A. E.; Engelhard, M. H.; Linford, M. R., Silicon (100)/SiO2 by XPS. *Surf. Sci. Spectra* **2013,** *20* (1), 36-42.

58. Yang, J. J.; Miao, F.; Pickett, M. D.; Ohlberg, D. A.; Stewart, D. R.; Lau, C. N.; Williams, R. S., The Mechanism of Electroforming of Metal Oxide Memristive Switches. *Nanotechnology* **2009,** *20* (21), 215201.

59. Avouris, P.; Martel, R.; Hertel, T.; Sandstrom, R., AFM-tip-induced and Current-induced Local Oxidation of Silicon and Metals. *Appl. Phys. A* **1998,** *66* (7), S659–S667.

60. Darwish, N.; Eggers, P. K.; Ciampi, S.; Tong, Y.; Ye, S.; Paddon-Row, M. N.; Gooding, J. J., Probing the Effect of the Solution Environment Around Redox-active Moieties Using Rigid Anthraquinone Terminated Molecular Rulers. *J. Am. Chem. Soc.* **2012,** *134* (44), 18401-18409.

61. Wind, R. A.; Jones, H.; Little, M. J.; Hines, M. A., Orientation-resolved Chemical Kinetics: Using Microfabrication to Unravel the Complicated Chemistry of KOH/Si Etching. *J. Phys. Chem. B* **2002,** *106* (7), 1557-1569.

62. James, M.; Ciampi, S.; Darwish, T. A.; Hanley, T. L.; Sylvester, S. O.; Gooding, J. J., Nanoscale Water Condensation on Click-functionalized Self-assembled Monolayers. *Langmuir* **2011,** *27* (17), 10753-10762.

63. Bougrini, M.; Baraket, A.; Jamshaid, T.; El Aissari, A.; Bausells, J.; Zabala, M.; El Bari, N.; Bouchikhi, B.; Jaffrezic-Renault, N.; Abdelhamid, E., Development of a Novel Capacitance Electrochemical Biosensor Based on Silicon Nitride for Ochratoxin A Detection. *Sens. Actuators B: Chem.* **2016,** *234*, 446-452.

64. Bahri, M.; Baraket, A.; Zine, N.; Ali, M. B.; Bausells, J.; Errachid, A., Capacitance Electrochemical Biosensor Based on Silicon Nitride Transducer for TNF-α Cytokine Detection in Artificial Human Saliva: Heart Failure (HF). *Talanta* **2020,** *209*, 120501.

65. Almadhoun, M. N.; Speckbacher, M.; Olsen, B. C.; Luber, E. J.; Sayed, S. Y.; Tornow, M.; Buriak, J. M., Bipolar Resistive Switching in Junctions of Gallium Oxide and P-type Silicon. *Nano Lett.* **2021,** *21* (6), 2666-2674.

66. Dief, E. M.; Darwish, N., Electrochemically Fabricated Molecule–Electrode Contacts for Molecular Electronics. *Curr. Opin. Electrochem.* **2022**, 101019.

67. Cohen, R.; Zenou, N.; Cahen, D.; Yitzchaik, S., Molecular Electronic Tuning of Si Surfaces. *Chem. Phys. Lett.* **1997,** *279* (5-6), 270-274.

68. Zhang, J.; Lin, S.; Wang, Z. L., Electrostatic Charges Regulate Chemiluminescence by Electron Transfer at the Liquid–Solid Interface. *J. Phys. Chem. B* **2022,** *126* (14), 2754-2760.

TOC graphic

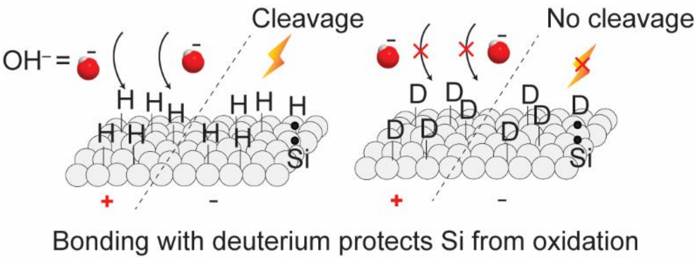

Bonding with deuterium protects Si from oxidation